The Astrophysical Journal, 660:256–266, 2007 May 1

DISSIPATIONLESS COLLAPSES IN MODIFIED NEWTONIAN DYNAMICS

Carlo Nipoti
Department of Astronomy, University of Bologna, I-40127 Bologna, Italy; carlo.nipoti@unibo.it

Pasquale Londrillo
INAF–Bologna Astronomical Observatory, I-40127 Bologna, Italy

and

Luca Ciotti
Department of Astronomy, University of Bologna, I-40127 Bologna, Italy
Received 2006 August 8; accepted 2007 January 12

ABSTRACT

Dissipationless collapses in modified Newtonian dynamics (MOND) are studied by using a new particle-mesh N-body code based on our numerical MOND potential solver. We found that low surface density end products have shallower inner density profiles, flatter radial velocity dispersion profiles, and more radially anisotropic orbital distributions than high surface density end products. The projected density profiles of the final virialized systems are well described by Sérsic profiles with index $m \lesssim 4$, down to $m \sim 2$ for a deep MOND collapse. Consistent with observations of elliptical galaxies, the MOND end products, if interpreted in the context of Newtonian gravity, would appear to have little or no dark matter within the effective radius. However, we found it impossible (under the assumption of constant stellar mass-to-light ratio) to simultaneously place the resulting systems on the observed Kormendy, Faber-Jackson, and fundamental plane relations of elliptical galaxies. Finally, the simulations provide strong evidence that phase mixing is less effective in MOND than in Newtonian gravity.

Subject headings: galaxies: elliptical and lenticular, cD — galaxies: formation — galaxies: kinematics and dynamics — gravitation — methods: numerical — stellar dynamics

1. INTRODUCTION

In Bekenstein & Milgrom's (1984, hereafter BM84) Lagrangian formulation of Milgrom's (1983) MOND, the Poisson equation

$$\nabla^2 \phi_{\rm N} = 4\pi G\rho \quad (1)$$

for the Newtonian gravitational potential $\phi_{\rm N}$ is replaced by the field equation

$$\nabla \cdot \left[\mu\left(\frac{\|\nabla\phi\|}{a_0}\right)\nabla\phi\right] = 4\pi G\rho, \quad (2)$$

where $a_0 \simeq 1.2 \times 10^{-10}$ m s^{-2} is a characteristic acceleration, $\|...\|$ is the standard Euclidean norm, ϕ is the MOND gravitational potential produced by the density distribution ρ, and in finite-mass systems $\nabla\phi \to 0$ for $\|\boldsymbol{x}\| \to \infty$. The MOND gravitational field $\boldsymbol{g}$ experienced by a test particle is

$$\boldsymbol{g} = -\nabla\phi, \quad (3)$$

and the function μ is such that

$$\mu(y) \sim \begin{cases} y, & y \ll 1, \\ 1, & y \gg 1; \end{cases} \quad (4)$$

throughout this paper we use

$$\mu(y) = \frac{y}{\sqrt{1+y^2}}. \quad (5)$$

In the so-called deep MOND regime (dMOND), describing low-acceleration systems ($\|\nabla\phi\| \ll a_0$), $\mu(y) = y$ and so equation (2) simplifies to

$$\nabla \cdot (\|\nabla\phi\|\nabla\phi) = 4\pi G a_0 \rho. \quad (6)$$

The source term in equation (2) can be eliminated by using equation (1), giving

$$\mu\left(\frac{\|\nabla\phi\|}{a_0}\right)\nabla\phi = \nabla\phi_{\rm N} + \boldsymbol{S}, \quad (7)$$

where $\boldsymbol{S} = \mathrm{curl}\,\boldsymbol{h}$ is a solenoidal field dependent on ρ and in general different from zero. When $\boldsymbol{S} = 0$ equation (7) reduces to Milgrom's (1983) formulation and can be solved explicitly. Such a reduction is possible for configurations with spherical, cylindrical, or planar symmetry, which are special cases of a more general family of stratifications (BM84; Brada & Milgrom 1995). Although the solenoidal field $\boldsymbol{S}$ has been shown to be small for some configurations (Brada & Milgrom 1995; Ciotti et al. 2006, hereafter CLN06), neglecting it when simulating time-dependent dynamical processes has dramatic effects such as nonconservation of total linear momentum (e.g., Felten 1984; see also § 3.1).

Nowadays some astronomical observational data appear consistent with the MOND hypothesis (see, e.g., Milgrom 2002; Sanders & McGaugh 2002). In addition, Bekenstein (2004) recently proposed a relativistic version of MOND (tensor-vector-scalar theory [TeVeS]), making it an interesting alternative to the cold dark matter paradigm. However, dynamical processes in MOND have been investigated very little so far, mainly due to difficulties posed by the nonlinearity of equation (2). Here we recall the spherically symmetric simulations (in which $\boldsymbol{S} = 0$)

of gaseous collapse in MOND by Stachniewicz & Kutschera (2005) and Nusser & Pointecouteau (2006). The only genuine three-dimensional MOND N-body simulations (in which eq. [2] is solved exactly) are those by Brada & Milgrom (1999, 2000), who studied the stability of disk galaxies and the external field effect, and those of Tiret & Combes (2007). Other attempts to study MOND dynamical processes have been conducted using three-dimensional N-body codes by arbitrarily setting $\boldsymbol{S} = 0$: Christodoulou (1991) investigated disk stability, while Nusser (2002) and Knebe & Gibson (2004) explored cosmological structure formation.[1]

In this paper we present results of N-body simulations of dissipationless collapse in MOND. The simulations were performed with an original three-dimensional particle-mesh N-body code, based on the numerical MOND potential solver presented in CLN06, which solves equation (2) exactly. These numerical experiments are interesting both from a purely dynamical point of view, allowing for the first time exploration of the relaxation processes in MOND, and in the context of elliptical galaxy formation. In fact, the ability of dissipationless collapse to produce systems strikingly similar to real elliptical galaxies is a remarkable success of Newtonian dynamics (e.g., van Albada 1982; Aguilar & Merritt 1990; Londrillo et al. 1991; Udry 1993; Trenti et al. 2005; Nipoti et al. 2006, hereafter NLC06), while there have been no indications so far that MOND can work as well in this respect. Here we study the structural and kinematical properties of the end products of MOND simulations, and we compare them with the observed scaling relations of elliptical galaxies: the Faber-Jackson (FJ) relation (Faber & Jackson 1976), the Kormendy (1977) relation, and the fundamental plane (FP) relation (Djorgovski & Davis 1987; Dressler et al. 1987).

The paper is organized as follows. The main features of the new N-body code are presented in § 2, while § 3 describes the setup and the analysis of the numerical simulations. The results are presented in § 4 and discussed in § 5.

2. THE N-BODY CODE

While most N-body codes for simulations in Newtonian gravity are based on the gridless multipole-expansion tree code scheme (Barnes & Hut 1986; see also Dehnen 2002), the nonlinearity of the MOND field equation (2) forces one to resort to other methods, such as the particle-mesh technique (see Hockney & Eastwood 1988). In this approach, particles are moved under the action of a gravitational field that is computed on a grid, with particle-mesh interpolation providing the link between the two representations. In our MOND particle-mesh N-body code, we adopt a spherical grid of coordinates (r, θ, φ), made of $N_r \times N_\theta \times N_\varphi$ points, on which the MOND field equation is solved as in CLN06. Particle-mesh interpolations are obtained with a quadratic spline in each coordinate, while time stepping is given by a classical leapfrog scheme (Hockney & Eastwood 1988). The time step Δt is the same for all particles and is allowed to vary adaptively in time. In particular, according to the stability criterion for the leapfrog time integration, we adopt $\Delta t = \eta/\left(\max|\nabla^2\phi|\right)^{1/2}$, where $\eta \lesssim 0.3$ is a dimensionless parameter. We found that $\eta = 0.1$ assures good conservation of the total energy in the Newtonian cases (see § 3.1). In the present version of the code, all the computations on the particles and the particle-mesh interpolations can be split among different processors, while the computations relative to the potential solver are not performed in parallel. The solution of equation (2) over the grid is then the bottleneck of the simulations: however, the iterative procedure on which the potential solver is based (see CLN06) allows one to adopt as a seed solution at each time step the previously determined potential.

The MOND potential solver can also solve the Poisson equation (obtained by imposing $\mu = 1$ in eq. [2]) so Newtonian simulations can be run with the same code. We exploited this property to test the code by running several Newtonian simulations of both equilibrium distributions and collapses, comparing the results with those of simulations (starting from the same initial conditions) performed with the FORTRAN version of fast Poisson solver (FVFPS) tree code (Londrillo et al. 2003; Nipoti et al. 2003). One of these tests is described in § 4.1.2.

We also verified that the code reproduces the Newtonian and MOND conservation laws (see § 3.1): note that the conservation laws in MOND present some peculiarities with respect to the Newtonian case, so we give here a brief discussion of the subject. As already stressed by BM84, equation (2) is obtained from a variational principle applied to a Lagrangian with all the required symmetries, so energy, and linear and angular momentum are conserved. Unfortunately, as also shown by BM84, the total energy diverges even for finite-mass systems, thus posing a computational challenge to code validation. We solved this problem by checking the volume-limited energy balance equation

$$\frac{d}{dt}\int_{V_0}\left[k + \rho\phi + \frac{a_0^2}{8\pi G}F\left(\frac{||\nabla\phi||}{a_0}\right)\right] d^3\boldsymbol{x} = \frac{1}{4\pi G}\int_{\partial V_0}\mu\frac{\partial\phi}{\partial t}\langle\nabla\phi, \hat{\boldsymbol{n}}\rangle\, da, \tag{8}$$

which is derived in Appendix A. In equation (8) V_0 is an arbitrary (but fixed) volume enclosing all the system mass, k is the kinetic energy per unit volume, and

$$F(y) \equiv 2\int_{y_0}^{y}\mu(\xi)\xi\, d\xi, \tag{9}$$

where y_0 is an arbitrary constant; note that only finite quantities are involved. Another important relation between global quantities for a system at equilibrium (in MOND as in Newtonian gravity) is the virial theorem

$$2K + W = 0, \tag{10}$$

where K is the total kinetic energy and $W = \mathrm{tr}\, W_{ij}$ is the trace of the Chandrasekhar potential energy tensor

$$W_{ij} \equiv -\int \rho(\boldsymbol{x})x_i\frac{\partial\phi(\boldsymbol{x})}{\partial x_j}\, d^3\boldsymbol{x} \tag{11}$$

(e.g., Binney & Tremaine 1987). Note that in MOND $K + W$ is *not* the total energy and is not conserved. However, *W is conserved in the limit of dMOND*, as $W = -(2/3)(Ga_0M_*^3)^{1/2}$ for *all* systems of finite total mass M_* (see Appendix B for the proof). As a consequence, in dMOND the virial theorem is simply $\sigma_V^4 = 4GM_*a_0/9$, where $\sigma_V \equiv (2K/M_*)^{1/2}$ is the system virial velocity dispersion (this relation was proved by Milgrom [1994]; see also Milgrom [1984] and Gerhard & Spergel [1992]). In our simulations we also tested that equation (10) is satisfied at equilibrium and that W is conserved in the dMOND case (see §§ 3.1 and 4).

3. NUMERICAL SIMULATIONS

The choice of appropriate scaling physical units is an important aspect of N-body simulations. This is especially true in the

[1] Cosmological N-body simulations in the context of a relativistic MOND theory such as TeVeS have not been performed so far.

TABLE 1
Time, Velocity, and Energy Units for N-Body Simulations

Newtonian and MOND	dMOND
$t_{*\mathrm{N}} = r_*^{3/2}(GM_*)^{-1/2}$	$t_{*d} = r_*(GM_*a_0)^{-1/4}$
$v_{*\mathrm{N}} = (GM_*)^{1/2}r_*^{-1/2}$	$v_{*d} = (GM_*a_0)^{1/4}$
$E_{*\mathrm{N}} = GM_*^2r_*^{-1}$	$E_{*d} = (Ga_0)^{1/2}M_*^{3/2}$

present case, in which we want to compare MOND and Newtonian simulations having the same initial conditions. As is well known, due to the scale-free nature of Newtonian gravity, a Newtonian N-body simulation starting from a given initial condition describes in practice ∞^2 systems of arbitrary mass and size. Each of them is obtained by assigning specific values to the length and mass units, r_* and M_*, respectively, in which the initial conditions are expressed. Also, dMOND gravity is scale free, because a_0 appears only as a multiplicative factor in equation (6), and so a simulation in dMOND gravity represents systems with arbitrary mass and size (although, in principle, the results apply only to systems with accelerations much smaller than a_0). MOND simulations can also be rescaled, but due to the presence of the characteristic acceleration a_0 in the nonlinear function μ, each simulation describes only ∞^1 systems, because r_* and M_* cannot be chosen independently of each other.

On the basis of the above discussion, we fix the physical units as follows (see Appendix C for a detailed description of the scaling procedure). Let the initial density distribution be characterized by a total mass M_* and a characteristic radius r_*. We rescale the field equations so that the dimensionless source term is the same in Newtonian, MOND, and dMOND simulations. We also require that the second law of dynamics, when cast in dimensionless form, is independent of the specific force law considered, and this leads to fixing the time unit. As a result, Newtonian and MOND simulations have the same time unit $t_{*\mathrm{N}} = r_*^{3/2}(GM_*)^{-1/2}$, while the natural time unit in dMOND simulations is $t_{*d} = r_*(GM_*a_0)^{-1/4}$. Note that MOND simulations are characterized by the dimensionless parameter $\kappa = GM_*/r_*^2a_0$ and scaling of a specific simulation is allowed provided the value of κ is maintained constant. Therefore, simulations with lower κ-values describe lower surface density, weaker acceleration systems; dMOND simulations represent the limiting case $\kappa \ll 1$, while Newtonian ones describe the regime with $\kappa \gg 1$. With the time units fixed, the corresponding velocity and energy units are $v_{*\mathrm{N}} \equiv r_*/t_{*\mathrm{N}}$, $v_{*d} \equiv r_*/t_{*d}$, and $E_{*\mathrm{N}} = M_*v_{*\mathrm{N}}^2$, $E_{*d} = M_*v_{*d}^2$, respectively (see Table 1 for a summary).

3.1. *Initial Conditions and Analysis of the Simulations*

We performed a set of five dissipationless-collapse N-body simulations, starting from the same phase-space configuration: the initial particle distribution follows the Plummer (1911) spherically symmetric density distribution

$$\rho(r) = \frac{3M_*r_*^2}{4\pi(r^2 + r_*^2)^{5/2}}, \tag{12}$$

where M_* is the total mass and r_* is a characteristic radius. The choice of a Plummer sphere as the initial condition is quite artificial and not necessarily the most realistic to reproduce initial conditions in the cosmological context (e.g., Gunn & Gott 1972). We adopt such a distribution to adhere to other papers dealing with collisionless collapse (e.g., Londrillo et al. 1991; NLC06; see also § 5, in which we present the results of a set of simulations starting from different initial conditions). The particles are at rest, so the initial virial ratio $2K/|W| = 0$. What is different in each simulation is the adopted gravitational potential, which is Newtonian in simulation N, dMOND in simulation D, and MOND with acceleration ratio κ in simulations Mκ ($\kappa = 1, 2, 4$). For each simulation we define the dynamical time t_{dyn} as the time at which the virial ratio $2K/|W|$ reaches its maximum value. In particular, we find $t_{\mathrm{dyn}} \sim 2t_{*d}$ in simulation D and $t_{\mathrm{dyn}} \sim 2t_{*\mathrm{N}}$ in simulations N, M1, M2, and M4. We note that $t_{\mathrm{dyn}} \sim GM_*^{5/2}(2|K + W|)^{-3/2}$ in simulation N.

Following NLC06, the particles are spatially distributed according to equation (12) and then randomly shifted in position (up to $r_*/5$ in modulus). This artificial, small-scale "noise" is introduced to enhance the phase mixing at the beginning of the collapse, because the numerical noise is small and the velocity dispersion is zero (see also § 4.2). As such, these fluctuations are not intended to reproduce any physical clumpiness.

All the simulations (realized with $N = 10^6$ particles, and a grid with $N_r = 64$, $N_\theta = 16$, and $N_\varphi = 32$) are evolved up $t = 150t_{\mathrm{dyn}}$. In all cases the modulus of the center-of-mass position oscillates around zero with rms $\lesssim 0.1r_*$; similarly, the modulus of the total angular momentum oscillates around zero[2] with rms $\lesssim 0.02$, in units of $r_*M_*v_{*\mathrm{N}}$ (simulations Mκ and N) and of $r_*M_*v_{*d}$ (simulation D). The quantity $K + W$ in the Newtonian simulation and W in the dMOND simulation are conserved to within 2% and 0.6%, respectively. The volume-limited energy balance equation (8) is conserved with an accuracy of 1% in MOND simulations, independent of the adopted V_0. To estimate possible numerical effects, we reran one of the MOND collapse simulations (M1) using $N = 2\times10^6$, $N_r = 80$, $N_\theta = 24$, and $N_\varphi = 48$: we found that the end products of these two simulations do not differ significantly, as far as the properties relevant to the present work are concerned.

The intrinsic and projected properties of the collapse end products are determined as in NLC06. In particular, the position of the center of the system is determined using the iterative technique described by Power et al. (2003). Following Nipoti et al. (2002), we measure the axis ratios c/a and b/a of the inertia ellipsoid (where a, b, and c are the major, intermediate, and minor axis, respectively) of the final density distributions, their angle-averaged profile, and their half-mass radius r_h. We fitted the final angle-averaged density profiles with the γ-model (Dehnen 1993; Tremaine et al. 1994)

$$\rho(r) = \frac{\rho_0 r_\mathrm{c}^4}{r^\gamma(r_\mathrm{c} + r)^{4-\gamma}}, \tag{13}$$

where the inner slope γ and the break radius r_c are free parameters, and the reference density ρ_0 is fixed by the total mass M_*. The fitting radial range is $0.06 \lesssim r/r_h \lesssim 10$. In order to estimate the importance of projection effects, for each end product we consider three orthogonal projections along the principal axes of the inertia tensor, measuring the ellipticity $\epsilon = 1 - b_e/a_e$, the circularized projected density profile, and the circularized effective radius $R_e \equiv (a_eb_e)^{1/2}$ (where a_e and b_e are the major and minor semi-axis, respectively, of the effective isodensity ellipse). We fitted (over the radial range $0.1 \lesssim R/R_e \lesssim 10$) the circularized

[2] As an experiment we also ran a simulation, with the same initial conditions and parameter κ as M1, in which the force was calculated from eq. (7), imposing $\boldsymbol{S} = 0$. In this simulation the linear and angular momentum are strongly not conserved: for instance, the center of mass is already displaced by $\sim 7r_*$ after $\sim 30t_{\mathrm{dyn}}$.

TABLE 2
End Product Properties

Simulation	κ	c/a	b/a	γ	r_c/r_h	m_a	m_b	m_c	ϵ_a	ϵ_b	ϵ_c
D	...	0.21	0.41	$0.17^{+0.39}_{-0.17}$	$0.27^{+0.09}_{-0.02}$	2.87 ± 0.01	2.50 ± 0.03	2.16 ± 0.02	0.48	0.80	0.58
M1	1	0.47	0.85	$1.24^{+0.40}_{-0.36}$	$0.44^{+0.20}_{-0.12}$	3.20 ± 0.07	3.00 ± 0.09	3.07 ± 0.13	0.42	0.51	0.17
M2	2	0.48	0.92	$1.45^{+0.26}_{-0.34}$	$0.53^{+0.19}_{-0.13}$	3.38 ± 0.08	3.24 ± 0.08	3.28 ± 0.12	0.49	0.45	0.08
M4	4	0.47	0.90	$1.54^{+0.26}_{-0.32}$	$0.58^{+0.20}_{-0.15}$	3.55 ± 0.10	3.40 ± 0.11	3.34 ± 0.15	0.51	0.45	0.10
N	...	0.45	0.91	$1.69^{+0.13}_{-0.15}$	$0.74^{+0.14}_{-0.12}$	4.21 ± 0.07	4.35 ± 0.08	3.96 ± 0.13	0.48	0.55	0.12
D′	...	0.25	0.45	$0.72^{+0.36}_{-0.50}$	$0.37^{+0.12}_{-0.11}$	3.06 ± 0.06	2.90 ± 0.04	2.71 ± 0.08	0.44	0.76	0.56
M′	20	0.42	0.83	$1.26^{+0.44}_{-0.40}$	$0.47^{+0.25}_{-0.15}$	3.41 ± 0.09	3.36 ± 0.06	3.20 ± 0.13	0.49	0.57	0.16
N′	...	0.45	0.93	$1.78^{+0.15}_{-0.18}$	$0.78^{+0.24}_{-0.18}$	4.29 ± 0.10	4.56 ± 0.15	4.19 ± 0.22	0.51	0.55	0.09

Notes.—First column: name of the simulation. The expression $\kappa = GM_*/r_*^2 a_0$: acceleration ratio; c/a and b/a: minor-to-major and intermediate-to-major axis ratios, respectively; γ, r_c: best-fit γ-model parameters; m_a, m_b, m_c, and ϵ_a, ϵ_b, ϵ_c: best-fit Sérsic indices and ellipticities, respectively, for projections along the principal axes.

projected density profiles of the end products with the $R^{1/m}$ Sérsic (1968) law:

$$I(R) = I_e \exp\left\{-b(m)\left[\left(\frac{R}{R_e}\right)^{1/m} - 1\right]\right\}, \qquad (14)$$

where $I_e \equiv I(R_e)$ and $b(m) \simeq 2m - 1/3 + 4/405m$ (Ciotti & Bertin 1999). In the fitting procedure m is the only free parameter, because R_e and I_e are determined by their measured values obtained by particle count. In addition, we measure the central velocity dispersion σ_0, obtained by averaging the projected velocity dispersion over the circularized surface density profile within an aperture of $R_e/8$. Some of these structural parameters are reported in Table 2 for the five simulations described above, as well as for three additional simulations, which start from different initial conditions (see § 5).

4. RESULTS

In Newtonian gravity, collisionless systems reach virialization through violent relaxation in a few dynamical times, as predicted by the theory (Lynden-Bell 1967) and confirmed by numerical simulations (e.g., van Albada 1982). On the other hand, due to the nonlinearity of the theory and the lack of numerical simulations, the details of relaxation processes and virialization in MOND are much less well known. Thus, before discussing the specific properties of the collapse end products, we present a general overview of the time evolution of the virial quantities in our simulations, postponing to § 4.2 a more detailed description of the phase-space evolution. In particular, in Figure 1 we show the time evolution of $2K/|W|$, K, W, and $K + W$ for simulations D, M1, and N. In the diagrams time is normalized to $t_{\rm dyn}$, so plots referring to different simulations are directly comparable (the values of $t_{\rm dyn}$ in time units for the five simulations are given in § 3.1). In simulation N (*right*) we find the well-known behavior of Newtonian dissipationless collapses: $2K/|W|$ has a peak, then oscillates, and eventually converges to the equilibrium value $2K/|W| = 1$; the total energy $K + W$ is nicely conserved during the collapse, although it presents a secular drift, a well-known feature of time integration in N-body codes. The time evolution of the same quantities is significantly different in a dMOND simulation (*left*). In particular, the virial ratio $2K/|W|$ quickly becomes close to 1 but is still oscillating at very late times because of the oscillations of K, while W is constant as expected. As we show in § 4.2, these oscillations are related to a peculiar behavior of the system in phase space. Finally, simulation M1 (*center*) represents an intermediate case between models N and D: the system starts as dMOND, but soon its core becomes concentrated enough to enter the Newtonian regime. After the initial phases of the collapse, Newtonian gravity acts effectively in damping the oscillations of the virial ratio. Overall, it is apparent how the system is in a "mixed" state, neither Newtonian ($K + W$ is not conserved) nor dMOND (W is not constant).

4.1. *Properties of the Collapse End Products*

4.1.1. *Spatial and Projected Density Profiles*

We found that all the simulated systems, once virialized, are not spherically symmetric. However, while the dMOND collapse end product is triaxial ($c/a \sim 0.2$, $b/a \sim 0.4$), MOND and Newtonian end products are oblate ($c/a \sim c/b \sim 0.5$). The ellipticity ϵ of the projected density distributions (measured for each of the principal projections) is found in the range 0.5–0.8 in D and 0–0.5 in M1, M2, M4, and N. These values are consistent with those observed in real elliptical galaxies, with the exception of ϵ_b in model D (see Table 2), which would correspond—if taken at face value—to an E8 galaxy. These results could be just due to the procedure adopted to measure the ellipticity (see § 3.1); however, we find it interesting that dMOND gravity could be able to produce some systems that would be unstable

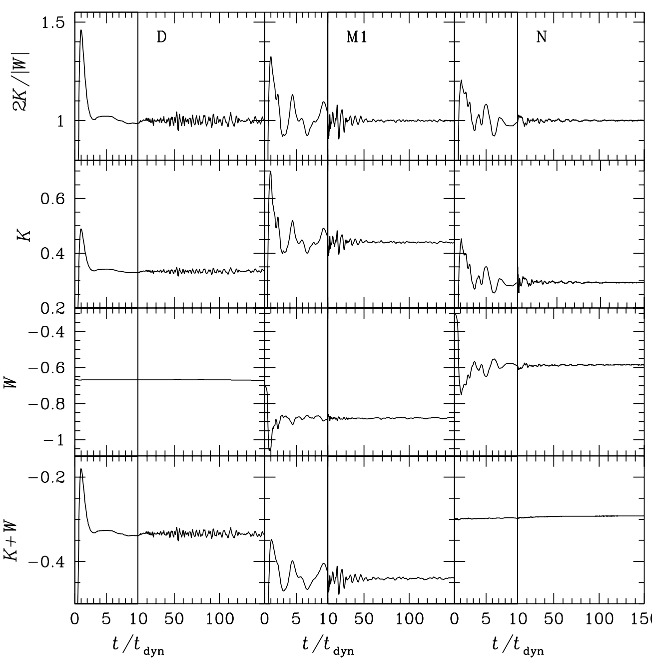

Fig. 1.—Time evolution of $2K/|W|$, K, W, and $K + W$ for simulations D, M1, and N. The K, W, and $K + W$ are in units of E_{*d} (*left*) and E_{*N} (*center and right*). For clarity, the time axes are zoomed in between 0 and 10.

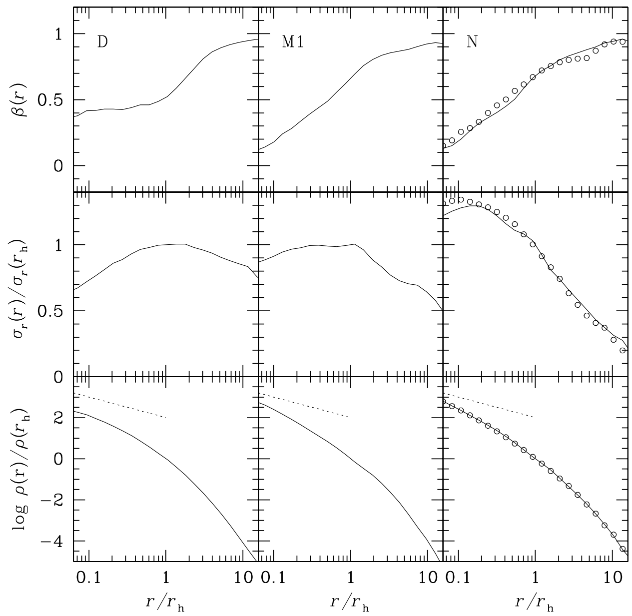

FIG. 2.—Angle-averaged density, radial velocity–dispersion, and anisotropy-parameter profiles (*from bottom to top*) for the end products of simulations D, M1, and N. Dotted lines in the bottom panels represent $\rho \propto r^{-1}$ profiles, which are shown for reference. Open circles in the right column show the corresponding profiles obtained with the FVFPS tree code from the same initial conditions.

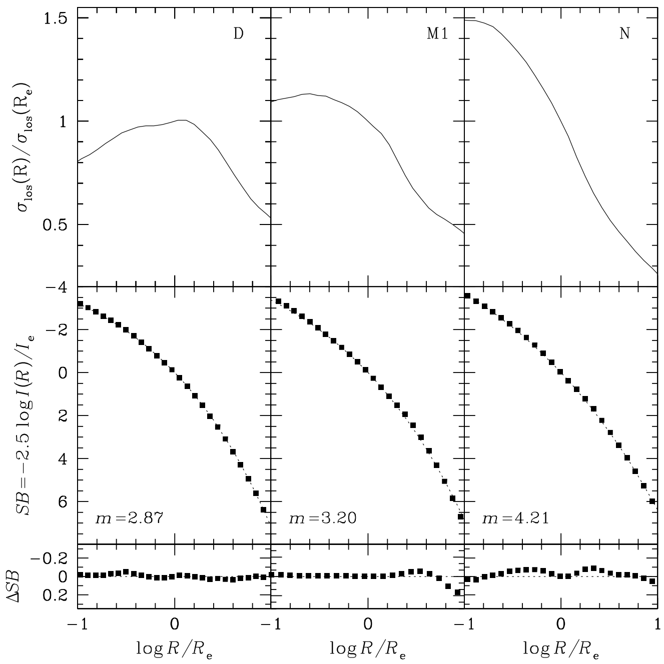

FIG. 3.—Line-of-sight velocity-dispersion profiles (*top*), circularized projected density profiles, and residuals of the Sérsic fit (*bottom*) of the end products of simulations D, M1, and N (*squares*; 1 σ error bars are always smaller than the symbol size). The dotted lines are the best-fitting Sérsic models.

in Newtonian gravity. We remark that a similar result, in the different context of disk stability in MOND, has been obtained by Brada & Milgrom (1999).

In order to describe the radial mass distribution of the final virialized systems, we fitted their angle-averaged density profiles with the γ-model (13) over the radial range $0.06 \lesssim r/r_h \lesssim 10$. The best-fit γ and r_c for the final distribution of each simulation are reported in Table 2 together with their 1 σ uncertainties (calculated from $\Delta\chi^2 = 2.30$ contours in the space γ-r_c). As also apparent from Figure 2 (*bottom*), the Newtonian collapse produced the system with the steepest inner profile ($\gamma \sim 1.7$), the dMOND end product has inner logarithmic slope close to zero, while MOND collapses led to intermediate cases, with γ ranging from $\sim$1.2 ($\kappa = 1$) to $\sim$1.5 ($\kappa = 4$). We also note that the ratio r_c/r_h (indicating the position of the knee in the density profile) increases systematically from dMOND to Newtonian simulations.

The circularized projected density profiles of the end products are analyzed as described in § 3.1. The best-fit Sérsic indices m_a, m_b, and m_c (for projections along the axes a, b, and c, respectively) are reported in Table 2, together with the 1 σ uncertainties corresponding to $\Delta\chi^2 = 1$; the relative uncertainties on the best-fit Sérsic indices are in all cases smaller than 5% and the average residuals between the data, and the fits are typically $0.05 \lesssim \langle \Delta SB \rangle \lesssim 0.2$, where $SB \equiv -2.5 \log\,[I(R)/I_e]$ is the surface brightness. The fitting radial range $0.1 \lesssim R/R_e \lesssim 10$ is comparable with or larger than the typical ranges spanned by observations (e.g., see Bertin et al. 2002). In agreement with previous investigations, we found that the Newtonian collapse produced a system well fitted by the de Vaucouleurs (1948) law. MOND collapses led to systems with Sérsic index $m < 4$, down to $m \sim 2$ in the case of the dMOND collapse. Figure 3 (*middle row*) shows the circularized (major axis) projected density profiles for the end products of simulations D, M1, and N, together with their best-fit Sérsic laws ($m = 2.87$, 3.20, and 4.21, respectively), and the corresponding residuals. Curiously, NLC06 found that low-m systems can be also obtained in Newtonian dissipationless collapses in the presence of a preexisting dark matter halo, with the Sérsic index value decreasing for increasing dark-to-luminous mass ratio.

4.1.2. *Kinematics*

We quantify the internal kinematics of the collapse end products by measuring the angle-averaged radial and tangential components (σ_r and σ_t) of their velocity-dispersion tensor, and the anisotropy parameter $\beta(r) \equiv 1 - 0.5\sigma_t^2/\sigma_r^2$. These quantities are shown in Figure 2 for simulations D, M1, and N. We note that the σ_r profile decreases more steeply in the Newtonian than in the MOND end products, while it presents a hole in the inner regions of the dMOND system. In addition, the dMOND galaxy is radially anisotropic ($\beta \sim 0.4$), even in the central regions, where models N and M1 are approximately isotropic ($\beta \sim 0.1$). All systems are strongly radially anisotropic for $r \gtrsim r_h$. For each model projection we computed the line-of-sight velocity dispersion σ_{los}, considering particles in a strip of width $R_e/4$ centered on the semimajor axis of the isophotal ellipse. The line-of-sight velocity-dispersion profiles (for the major-axis projection) are plotted in the top panels of Figure 3. The Newtonian profile is very steep within R_e, while MOND and dMOND profiles are significantly flatter there. As well as σ_r, σ_{los} decreases for decreasing radius in the inner region of model D. The kinematical properties of M2 and M4 are intermediate between those of M1 and of N: overall we find only weak dynamical nonhomology among MOND end products. The open symbols in Figure 2 (*right*) refer to a test Newtonian simulation run with the FVFPS tree code (with 4×10^5 particles). The structural and kinematical properties of the end product of this simulation are clearly in good agreement with those of the end product of simulation N (*solid lines*), which started from the same initial conditions.

4.2. *Phase-Space Properties of MOND Collapses*

To explore the phase-space evolution of the systems during the collapse and the following relaxation, we consider time snapshots

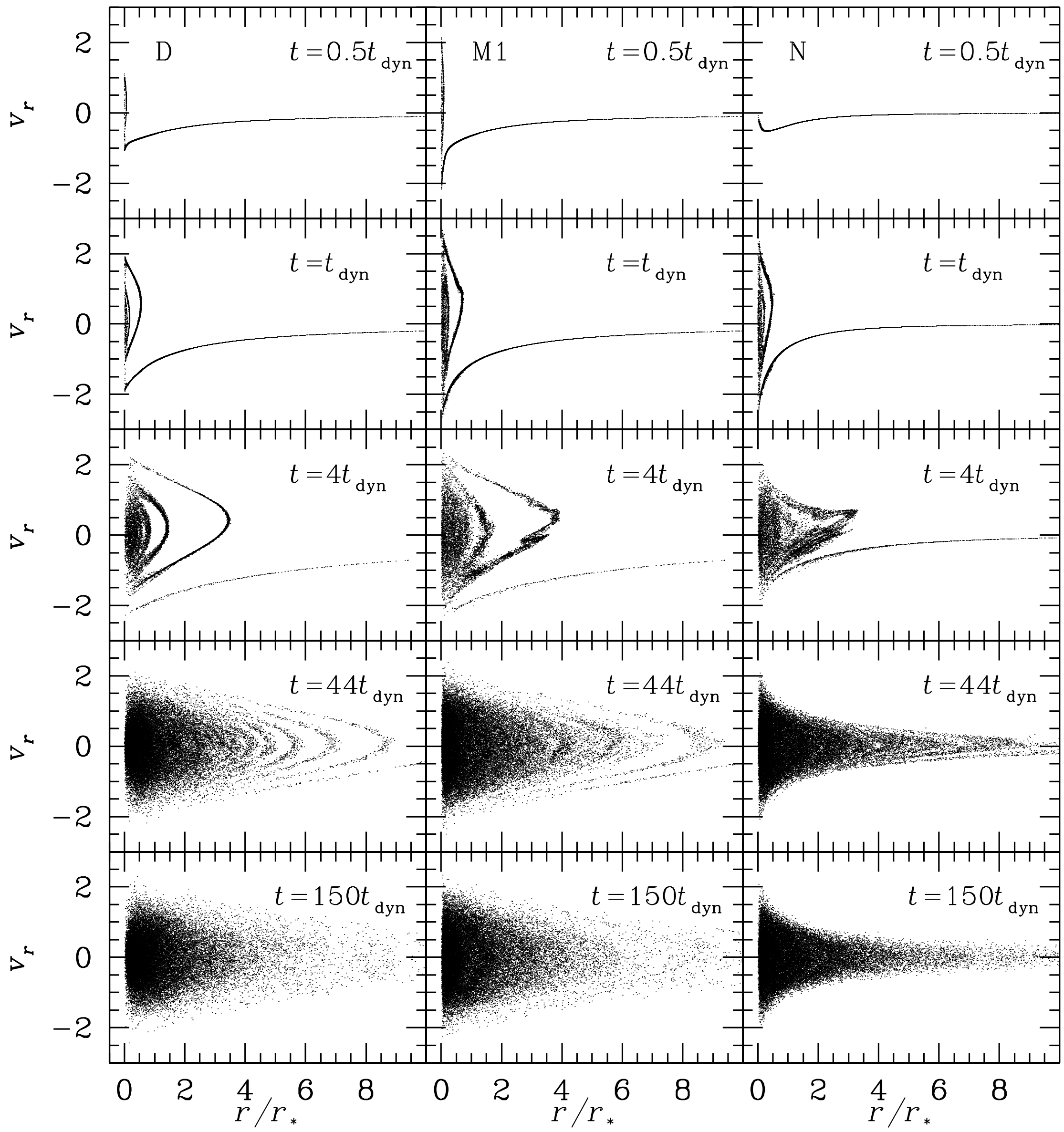

FIG. 4.—Phase-space (radial velocity vs. radius) diagrams for simulations D, M1, and N at various times. The quantity v_r is in units of v_{*d} (simulation D) and $v_{*\rm N}$ (simulations M1 and N; see Table 1).

of the particles' radial velocity (v_r) versus radius, as in Londrillo et al. (1991). In Figure 4 we plot five of these diagrams for simulations D, M1, and N: each plot shows the phase-space coordinates of 32,000 particles randomly extracted from the corresponding simulation, and as in Figure 1, times are normalized to the dynamical time $t_{\rm dyn}$ (see § 3.1). At time $t = 0.5t_{\rm dyn}$ all particles are still collapsing in simulation N, while in MOND simulations a minority of particles have already crossed the center of mass, as revealed by the vertical distribution of points at $r \sim 0$ in panels D and M1. At $t = t_{\rm dyn}$ (time of the peak of $2K/|W|$ in the three models), sharp shells in phase space are present, indicating that particles are moving in and out collectively and phase mixing has not taken place yet. At $t = 4t_{\rm dyn}$ is already apparent that phase mixing is operating more efficiently in simulation N than in simulation M1, while there is very little phase mixing in the dMOND collapse. At significantly late times ($t = 44t_{\rm dyn}$), when the three systems are almost virialized ($2K/|W| \sim 1$; see Figure 1), phase mixing is complete in simulation N, but phase-space shells still survive in models M1 and D. Finally, the bottom panels show the phase-space diagrams at equilibrium ($t = 150t_{\rm dyn}$), when phase mixing is completed also in the MOND and dMOND galaxies: note that the populated region in the (r, v_r) space is significantly different in MOND and in Newtonian gravity, which is consistent with the sharper decline of radial velocity dispersion in the Newtonian system.

Thus, our results indicate that phase mixing is more effective in Newtonian gravity than in MOND.[3] It is then interesting to estimate in physical units the phase-mixing timescales of MOND systems. From Table 1 it follows that $t_{*\rm N} \simeq 4.7(r_*/{\rm kpc})^{3/2} \times (M_*/10^{10}\ M_\odot)^{-1/2}$ Myr $= 29.8\kappa^{-3/4}(M_*/10^{10}\ M_\odot)^{1/4}$ Myr for $a_0 = 1.2 \times 10^{-10}$ m s^{-2}. For example, in the case of model M1, adopting $M_* = 10^{12}\ M_\odot$ [and $r_* = (GM_*/a_0)^{1/2} \simeq 34$ kpc], shells

[3] Ciotti et al. (2007) found similar results in "ad hoc" numerical simulations in which the angular force components were frozen to zero, so that the evolution was driven by radial forces only. In fact, while phase mixing is less effective both in MOND and in Newtonian simulations with respect to the simulations here reported, the phase-mixing timescale in MOND is still considerably longer than in Newtonian gravity.

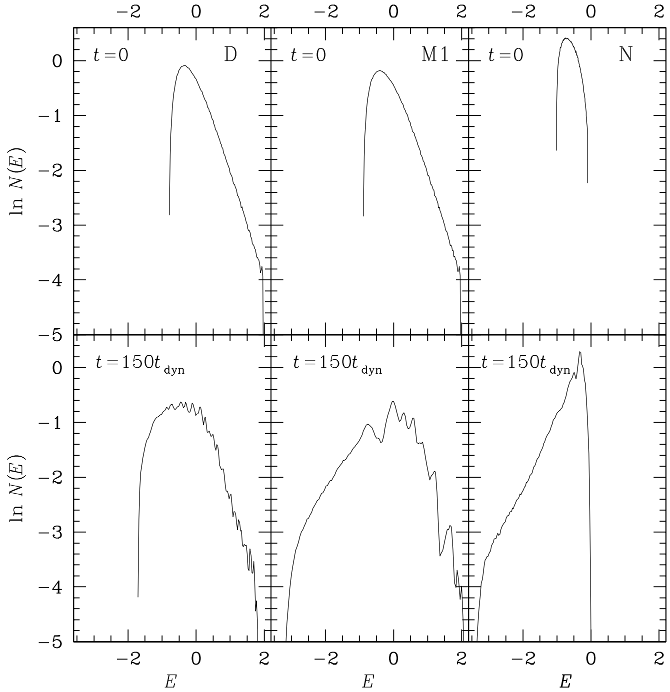

FIG. 5.—Initial (*top*) and final (*bottom*) differential energy distributions. The energy per unit mass E is in units of E_{*d}/M_* (model D) and E_{*N}/M_* (models M1 and N). The energy zero points in models D and M1 are such that the most bound particles of the M1 and N end products have the same energy and the highest energy particles of models D and M1 at $t = 0$ have the same energy.

in phase space are still apparent after $\sim$8.3 Gyr ($\simeq 44 t_{\rm dyn}$). Simulation M1 might also be interpreted as representing a dwarf elliptical galaxy of, say, $M_* = 10^9\ M_\odot$ [and $r_* = (GM_*/a_0)^{1/2} \simeq$ 1.1 kpc]. In this case $44 t_{\rm dyn} \sim 1.5$ Gyr. We conclude that in some MOND systems substructures in phase space can survive for significantly long times.

In addition to the (r, v_r) diagram, another useful diagnostic to investigate phase-space properties of gravitational systems is the energy distribution $N(E)$ (i.e., the number of particles with energy per unit mass between E and $E + dE$; e.g., Binney & Tremaine 1987; Trenti & Bertin 2005). Independently of the force law, the energy per unit mass of a particle orbiting at $\boldsymbol{x}$ with speed v in a gravitational potential $\phi(\boldsymbol{x})$ is $E = v^2/2 + \phi(\boldsymbol{x})$, and E is constant if ϕ is time-independent. In Newtonian gravity ϕ is usually set to zero at infinity for finite-mass systems, so $E < 0$ for bound particles; in MOND all particles are bound, independently of their velocity, because ϕ is confining and all energies are admissible. This difference is reflected in Figure 5, which plots the initial (*top*) and final (*bottom*) differential energy distributions for simulations D, M1, and N. Given that the particles are at rest at $t = 0$, the initial $N(E)$ depends only on the structure of the gravitational potential and is significantly different in the Newtonian and MOND cases. We also note that $N(E)$ is basically the same in models D and M1 at $t = 0$, because model M1 is initially in the dMOND regime. In accordance with previous studies, in the Newtonian case the final differential $N(E)$ is well represented by an exponential function over most of the populated energy range (Binney 1982; van Albada 1982; Ciotti 1991; Londrillo et al. 1991; NLC06). In contrast, in model D the final $N(E)$ decreases for increasing energy, qualitatively preserving its initial shape. In the case of simulation M1 there is an apparent dichotomy between a Newtonian part at lower energies (more bound particles), where $N(E)$ is exponential, and a dMOND part at higher energies, where the final $N(E)$ resembles the initial one. We interpret this result as another manifestation of a less effective phase-space reorganization in MOND than in Newtonian collapses.

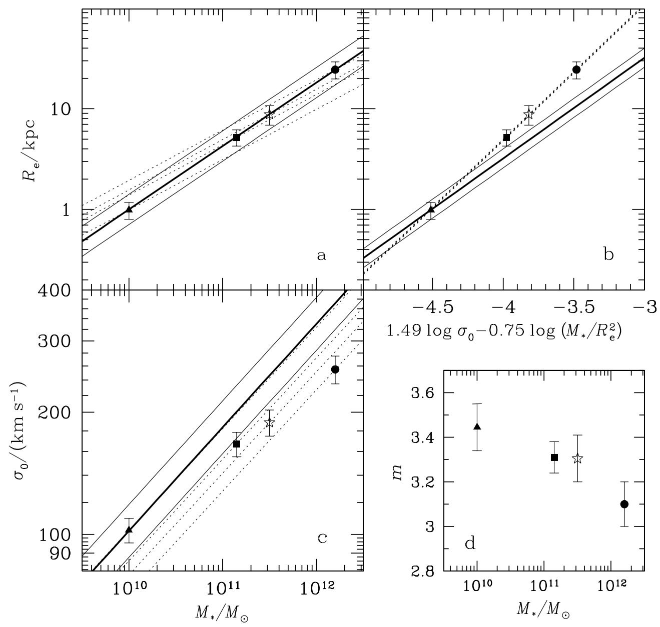

FIG. 6.—Location of the end products M1 (*circles*), M2 (*squares*), M4 (*triangles*), and M$'$ (*stars*) in the planes (*a*) M_*-R_e, (*c*) M_*-σ_0, (*d*) M_*-m, and in the plane (*b*) in which the FP is seen edge-on. Vertical bars account for the projection effects, while the filled symbols refer to average values between the two extremes. The thick solid lines represent the observed (*a*) Kormendy, (*c*) FJ, and (*b*) FP relations, and the thin solid lines give estimates of the corresponding scatter (Bernardi et al. 2003a, 2003b). The normalization is such that $R_e \simeq 4$ kpc for stellar mass $M_* = 10^{11}\ M_\odot$ (Shen et al. 2003). See text for the meaning of the dotted lines.

4.3. *Comparison with the Observed Scaling Relations of Elliptical Galaxies*

It is not surprising that galaxy scaling relations represent an even stronger test for MOND than for Newtonian gravity, due to the absence of dark matter and the existence of the critical acceleration a_0 with a universal value in the former theory (e.g., see Milgrom 1984; Sanders 2000). For example, when interpreting the FP tilt in Newtonian gravity one can invoke a systematic and fine-tuned increase of the galaxy dark-to-luminous mass ratio with luminosity (e.g., Bender et al. 1992; Renzini & Ciotti 1993; Ciotti et al. 1996), while in MOND the tilt should be related to the characteristic acceleration a_0. Note, however, that in MOND, as well as in Newtonian gravity, other important physical properties may help to explain the FP tilt, such as a systematic increase of radial orbital anisotropy with mass or a systematic structural weak homology (Bertin et al. 2002). Due to the relevance of the subject, we attempt here to derive some preliminary hints. In particular, for the first time, we can compare with the scaling relations of elliptical galaxies MOND models produced by a formation mechanism, even though the considered formation mechanism (dissipationless collapse) is quite simple.

In this section we consider the end products of simulations M1, M2, and M4. As already discussed in § 3, each of the three systems corresponds to a family with constant M_*/r_*^2. This degeneracy is represented by the straight dotted lines in Figure 6*a*: all galaxies on the same dotted line have the same κ-value. This behavior is very different from the Newtonian case, in which the result of a N-body simulation can be placed anywhere in the space R_e-M_*, by arbitrarily choosing M_* and r_*. For comparison with observations, the specific scaling laws represented in Figure 6 (*thick solid lines*) are the near-infrared r^*-band Kormendy relation $R_e \propto M_*^{0.63}$, the FJ relation $M_* \propto \sigma_0^{3.91}$ (Bernardi et al. 2003a), and the edge-on FP relation in the same band $\log R_e = A \log \sigma_0 + B \log (M_*/R_e^2) + \text{const.}$ (with $A = 1.49$, $B = -0.75$; Bernardi et al. 2003b), under the assumption of a luminosity-independent stellar mass-to-light ratio.

The physical properties of each model are determined as follows. First, for each model (identified by a value of $\kappa = GM_*/r_*^2 a_0$) we measure the ratio R_e/r_* (see § 3.1), and so we obtain $R_e = R_e(\kappa, M_*)$. This function, for fixed κ and variable M_*, is a dotted line in Figure 6*a*. As apparent, only one pair (R_e, M_*) satisfies the Kormendy relation for each κ: in particular, we obtain that models M1, M2, and M4 have stellar masses 1.6×10^{12}, 1.4×10^{11}, and 10^{10} $M_\odot$, respectively (so lower κ models correspond to higher mass systems). We are now in the position to obtain $r_* = (GM_*/a_0\kappa)^{1/2}$ and $v_{*\mathrm{N}} = (\kappa a_0 G M_*)^{1/4}$; thus, we know the physical value of the projected central velocity dispersion, and we can place our models also in the FJ and FP planes. It is apparent that these two relations are not reproduced, in particular, by massive galaxies. We note that this discrepancy cannot be fixed even when considering the mass interval allowed by the scatter in the Kormendy relation (Fig. 6*a*, *thin solid lines*), as revealed by the dotted lines in Figures 6*b* and 6*c*, which are just the projections of the dotted lines in Figure 6*a* onto the planes of the edge-on FP[4] and the FJ. Finally, Figure 6*d* plots the best-fit Sérsic index m of the models as a function of M_*. Observations show that elliptical galaxies are characterized by m-values increasing with size: $m \gtrsim 4$ for galaxies with $R_e \gtrsim 3$ kpc and $m \lesssim 4$ for those with $R_e \lesssim 3$ kpc (e.g., Caon et al. 1993). Our models behave in the opposite way, as m decreases for increasing size (mass) of the system. So, while model M4 ($R_e \sim 1$ kpc, $m \sim 3.4$) is consistent with observations, models M1 and M2 have significantly lower m than real elliptical galaxies of comparable size. However, this finding is not a peculiarity of MOND gravity: also in Newtonian gravity dissipationless collapse end products with $m > 4$ are obtained only for specific initial conditions (NLC06), while equal-mass Newtonian mergings are able to produce high-m systems (Nipoti et al. 2003).

So far we have compared the results of our simulations with the scaling relations of high surface brightness galaxies. However, it is well known that low surface brightness, hot stellar systems, such as dwarf elliptical galaxies and dwarf spheroidal galaxies, have larger effective radii than predicted by the Kormendy relation (e.g., Bender et al. 1992; Capaccioli et al. 1992; Graham & Guzmán 2003). In particular, dwarf elliptical galaxies are characterized by effective surface densities comparable to those of the most luminous elliptical galaxies, while their surface brightness profiles are characterized by Sérsic indices smaller than 4 (e.g., Caon et al. 1993; Trujillo et al. 2001). Dwarf spheroidal galaxies are the lowest surface-density stellar systems known, and typically have exponential ($m \sim 1$) luminosity profiles (e.g., Mateo 1998). So, simulations M1 and D can be interpreted as modeling a dwarf elliptical and a dwarf spheroidal galaxy, respectively, and their end products qualitatively reproduce the surface brightness profiles of the observed systems. As pointed out in § 4.1.2, the velocity-dispersion profile of model D is rather flat, with a hole in the central regions: interestingly, observations of dwarf spheroidal galaxies indicate that their velocity-dispersion profiles are also flat (e.g., Walker et al. 2006 and references therein).

[4] In Fig. 6*b* the dotted lines are nearly coincident because (1) the models are almost homologous and (2) the variable in the abscissa is independent of κ, as the FP coefficients $A \sim -2B$ in this case.

5. DISCUSSION AND CONCLUSIONS

In this paper we studied the dissipationless collapse in MOND by using a new three-dimensional particle-mesh N-body code, which solves the MOND field equation (2) exactly. For obvious computational reasons, we did not attempt a complete exploration of the parameter space, and we just presented results of a small set of numerical simulations, ranging from Newtonian to dMOND systems. The main results of the present study can be summarized as follows:

1. The intrinsic structural and kinematical properties of the MOND collapse end products depend weakly on their characteristic surface density: lower surface-density systems have shallower inner density profiles, flatter velocity-dispersion profiles, and more radially anisotropic orbital distributions than higher surface-density systems.
2. The projected density profiles of the MOND collapse end products are characterized by Sérsic index m lower than 4, and decreasing indexes for decreasing mean surface density. In particular, the end product of the dMOND collapse, modeling a very low surface density system, is characterized by a Sérsic index $m \sim 2$ and by a central hole in the projected velocity-dispersion profile.
3. We found it impossible to satisfy simultaneously the observed Kormendy, Faber-Jackson, and fundamental plane relations of elliptical galaxies with the MOND collapse end products, under the assumption of a luminosity-independent mass-to-light ratio. In other words, this point and the two points above show that, in the framework of dissipationless collapse, the presence of a characteristic acceleration is not sufficient to reproduce important observed properties of spheroids of different mass and surface density, such as their scaling relations and weak structural homology.
4. From a dynamical point of view we found that phase mixing is less effective (and stellar systems take longer to relax) in MOND than in Newtonian gravity.

A natural question to ask is how the end products of our simulations would be interpreted in the context of Newtonian gravity. Clearly, models D and N would represent dark matter– and baryon-dominated stellar systems, respectively. More interestingly, models M1, M2, and M4, once at equilibrium, would be characterized by a *dividing radius*, separating a baryon-dominated inner region (with accelerations higher than a_0) from a dark matter–dominated outer region (with accelerations lower than a_0). This radius is $\sim 1.1 r_h$ for M1, $\sim 1.8 r_h$ for M2, and $\sim 2.7 r_h$ for M4. So, all these models would show little or no dark matter in their central regions. Remarkably, observational data indicate that there is at most as much dark matter as baryonic matter within the effective radius of elliptical galaxies (e.g., Bertin et al. 1994; Cappellari et al. 2006 and references therein).

The conclusions above have been drawn by considering only simulations starting from a Plummer density distribution. To explore the dependence of these results on this specific choice, we ran also three simulations starting from a cold ($2K/|W| = 0$), truncated density distribution $\rho(r) = CM_*/(r_*^3 + r^3)$, where $C^{-1} \equiv 4\pi \ln(1 + r_t^3/r_*^3)/3$, M_* is the total mass, and $r_t = 20 r_*$ is the truncation radius. Small-scale noise is introduced as described in § 3.1. Note that in the external parts the new initial conditions are significantly flatter than a Plummer sphere. The three simulations are labeled D′ (dMOND), M′ (MOND with acceleration ratio $\kappa = 20$),[5] and N′ (Newtonian). As in the case of Plummer initial conditions, in these cases the final intrinsic and projected density distributions are also well represented by γ-models and Sérsic models, respectively. In analogy with model N, the Newtonian collapse N′ produced the system with the steepest central density distribution (see Table 2). In addition, model M′, when compared with the scaling laws of elliptical galaxies (stars in Fig. 6), follows the same trend as models M1, M2, and M4. The analysis of the time evolution in phase space of models D′, M′, and N′ confirmed that mixing and relaxation processes are less effective in MOND than in Newtonian gravity.

How do the presented results depend on the specific choice (eq. [5]) of the MOND interpolating function μ? Recently, a few other interpolating functions have been proposed to better fit galactic rotation curves (Famaey & Binney 2005) and in the context of TeVeS (Bekenstein 2004; Zaho & Famaey 2006). It is reasonable to expect that the exact form of μ is not critical in a violent dynamical process such as dissipationless collapse. We verified that this is actually the case, by running an additional MOND simulation with the same initial conditions and parameter κ as simulation M1, but adopting $\mu(y) = y/(1 + y)$, as proposed by Famaey & Binney (2005). In fact, neither in the time evolution nor in the structural and kinematical properties of the end products did we find significant differences between the two simulations. This result suggests that, in the context of structure formation in MOND, the crucial feature is the presence of a characteristic acceleration separating the two gravity regimes, while the details of the transition region are unimportant.

Though the dissipationless collapse is a very simplistic model for galaxy formation, it is expected to describe reasonably well the last phase of ''monolithic-like'' galaxy formation, in which star formation is almost completed during the initial phases of the collapse. The importance of gas dissipation in the formation of elliptical galaxies is very well known, going back to the seminal works of Rees & Ostriker (1977) and White & Rees (1978; see also Ciotti et al. [2007], and references therein, for a discussion of the expected impact of gas dissipation on the scaling laws followed by elliptical galaxies). This aspect has been completely neglected in our exploration, and we are working on an hybrid (stars plus gas) version of the MOND code to explore quantitatively this issue. We also stress that the dissipationless collapse process catches the essence of violent relaxation, which is certainly relevant to the formation of spheroids even in more complicated scenarios, such as merging. For example, it is well known that in Newtonian dynamics systems with de Vaucouleurs profiles are produced by dissipationless merging of spheroids (e.g., White 1978) or disk galaxies (e.g., Barnes 1992), as well as by dissipationless collapses (van Albada 1982). Merging simulations in MOND have not been performed so far, and a relevant and still open question is how efficient merging is in MOND, in which the important effect of dark matter halos is missing and galaxies are expected to collide at higher speed than in Newtonian gravity (Binney 2004; Sellwood 2004). Our results, indicating that relaxation takes longer in MOND than in Newtonian gravity, go in the direction of making merging timescales even longer in MOND; on the other hand, analytical estimates seem to indicate shorter dynamical friction timescales in MOND than in Newtonian gravity (Ciotti & Binney 2004). Therefore, the next application of our code will be the study of galaxy merging in MOND.

[5] This value of κ is not directly comparable with those in simulations M1, M2, and M4, because of the different role of r_* in the corresponding initial distributions.

We are grateful to James Binney and Scott Tremaine for helpful discussions and to the anonymous referee for useful comments. This work was partially supported by the MIUR grant CoFin2004.

APPENDIX A

THE VOLUME-LIMITED ENERGY-BALANCE EQUATION IN MOND

In this appendix we derive a useful volume-limited integral relation representing energy conservation in MOND, which is well suited for testing numerical simulations. The total (ordered and random) kinetic energy per unit volume of a continuous distribution with density ρ and velocity field $\boldsymbol{u}$ is

$$k = \frac{\rho}{2}(||\boldsymbol{u}||^2 + \mathrm{tr}\,\sigma_{ij}^2), \tag{A1}$$

where σ_{ij}^2 is the velocity-dispersion tensor. In the present case the energy-balance equation is (e.g., Ciotti 2000)

$$\frac{d}{dt}\int_{V(t)} k\, d^3\boldsymbol{x} = -\int_{V(t)} \rho\boldsymbol{u} \cdot \nabla\phi\, d^3\boldsymbol{x}, \tag{A2}$$

where the integral in the right-hand side is the work per unit time done by mechanical forces. By application of the Reynolds transport theorem and using the mass continuity equation we obtain

$$\frac{\partial}{\partial t}(k + \rho\phi) + \nabla \cdot [(k + \rho\phi)\boldsymbol{u}] = \rho\frac{\partial\phi}{\partial t}. \tag{A3}$$

When ϕ is the MOND gravitational potential, ρ can be eliminated using equation (2), so

$$4\pi G\rho\frac{\partial\phi}{\partial t} = \nabla \cdot (\mu\nabla\phi)\frac{\partial\phi}{\partial t} = \nabla \cdot \left(\mu\nabla\phi\frac{\partial\phi}{\partial t}\right) - \frac{a_0^2}{2}\frac{\partial}{\partial t}\left[F\left(\frac{||\nabla\phi||}{a_0}\right)\right], \tag{A4}$$

where F is defined in equation (9). Thus, equation (A3) can be written as

$$\frac{\partial}{\partial t}\left[k+\rho\phi+\frac{a_0^2}{8\pi G}F\left(\frac{||\nabla\phi||}{a_0}\right)\right]+\nabla\cdot\left[(k+\rho\phi)\boldsymbol{u}-\frac{\mu\nabla\phi}{4\pi G}\frac{\partial\phi}{\partial t}\right]=0. \tag{A5}$$

By integration over a fixed control volume V_0 enclosing all the system mass, one obtains equation (8).

APPENDIX B

THE VIRIAL TRACE W IN DEEP MOND SYSTEMS OF FINITE MASS

Here we prove that $W=-(2/3)\left(Ga_0M_*^3\right)^{1/2}$ for any dMOND system of finite mass M_*. Eliminating ρ from equation (11) by using equation (6), and considering the trace of the resulting expression, one finds

$$W=-\frac{1}{4\pi Ga_0}\int D[\phi]\nabla\cdot(\|\nabla\phi\|\nabla\phi)\,d^3\boldsymbol{x}, \tag{B1}$$

where we define the operator $D\equiv\langle\boldsymbol{x},\nabla\rangle$. The remarkable fact behind the proof is that the integrand above can be written as the divergence of a vector field, so only contributions from $r\to\infty$ are important. We will then use the spherically symmetric asymptotic behavior of dMOND solutions for $r\to\infty$ (BM84),

$$\boldsymbol{g}=-\nabla\phi\sim-\frac{\sqrt{GM_*a_0}}{r}\hat{\boldsymbol{e}}_r, \tag{B2}$$

and Gauss's theorem to evaluate W.

Theorem.—For a generic potential the following identity holds:

$$D[\phi]\nabla\cdot(\|\nabla\phi\|\nabla\phi)=\nabla\cdot\left(D[\phi]\|\nabla\phi\|\nabla\phi-\frac{\boldsymbol{x}\|\nabla\phi\|^3}{3}\right). \tag{B3}$$

Proof.—From standard vector analysis (e.g., Jackson 1999) it follows that

$$D[\phi]\nabla\cdot(\|\nabla\phi\|\nabla\phi)=\nabla\cdot(D[\phi]\|\nabla\phi\|\nabla\phi)-\|\nabla\phi\|\langle\nabla\phi,\nabla D[\phi]\rangle \tag{B4}$$

and

$$\|\nabla\phi\|\langle\nabla\phi,\nabla D[\phi]\rangle=\frac{\nabla\cdot\left(\boldsymbol{x}\|\nabla\phi\|^3\right)}{3}. \tag{B5}$$

Identity (B5) follows from the expansion $\nabla D[\phi]=\nabla\phi+D[\nabla\phi]$ as

$$\|\nabla\phi\|^3+\|\nabla\phi\|\langle\nabla\phi,D[\nabla\phi]\rangle=\|\nabla\phi\|^3+\frac{D\left[\|\nabla\phi\|^3\right]}{3}=\frac{\nabla\cdot\left(\boldsymbol{x}\|\nabla\phi\|^3\right)}{3}. \tag{B6}$$

Combining equations (B4) and (B5) completes the proof of equation (B3).

We now transform the volume integral (B1) into a surface integral over a sphere of radius r, and we consider the limit for $r\to\infty$, together with the asymptotic relation (B2), obtaining

$$W=-\frac{1}{4\pi Ga_0}\lim_{r\to\infty}\int_{4\pi}\frac{2}{3}r^3g^2\,d\Omega=-\frac{2}{3}\sqrt{Ga_0M_*^3}. \tag{B7}$$

APPENDIX C

SCALING OF THE EQUATIONS

Given a generic density distribution ρ, and the mass and length units M_* and r_*, we define the dimensionless quantities $\tilde{\boldsymbol{x}}\equiv\boldsymbol{x}/r_*$ and $\tilde{\rho}\equiv\rho r_*^3/M_*$. From equation (3) the equation of motion for a test particle can be written in dimensionless form as

$$\frac{d^2\tilde{\boldsymbol{x}}}{d\tilde{t}^2}=-\frac{\phi_*t_*^2}{r_*^2}\tilde{\nabla}\tilde{\phi}, \tag{C1}$$

where ϕ_* and t_* are for the moment two unspecified scaling constants, $\tilde{\phi} = \phi/\phi_*$ and $\tilde{t} = t/t_*$, and the dimensionless gradient operator is $\tilde{\nabla} = r_* \nabla$. In all of our simulations we define $t_* \equiv r_*/\phi_*^{1/2}$, so that the scaling factor in equation (C1) is unity, while ϕ_* is specified case-by-case from the field equation as follows.

In Newtonian gravity the Poisson equation (1) can be written as

$$\tilde{\nabla}^2 \tilde{\phi} = 4\pi \frac{GM_*}{r_* \phi_*} \tilde{\rho}; \tag{C2}$$

we fix $\phi_* = GM_*/r_*$, so $t_* = \left(r_*^3/GM_*\right)^{1/2} \equiv t_{*\mathrm{N}}$. The dMOND field equation (6) in dimensionless form is written

$$\tilde{\nabla} \cdot \left(||\tilde{\nabla}\tilde{\phi}||\tilde{\nabla}\tilde{\phi}\right) = 4\pi \frac{GM_* a_0}{\phi_*^2} \tilde{\rho}; \tag{C3}$$

thus, the natural choice is $\phi_* = (GM_* a_0)^{1/2}$ and $t_* = r_*(GM_* a_0)^{-1/4} \equiv t_{*d}$. Finally, the MOND field equation (2) in dimensionless form is

$$\tilde{\nabla} \cdot \left[\mu\left(\kappa||\tilde{\nabla}\tilde{\phi}||\right)\tilde{\nabla}\tilde{\phi}\right] = 4\pi \frac{GM_*}{r_* \phi_*} \tilde{\rho}, \tag{C4}$$

where $\kappa \equiv \phi_*/r_* a_0$. In this case, as in the Newtonian case, $\phi_* = GM_*/r_*$; therefore, $t_* = t_{*\mathrm{N}}$ and $\kappa = GM_*/r_*^2 a_0$.

REFERENCES

Aguilar, L. A., & Merritt, D. 1990, ApJ, 354, 33
Barnes, J. 1992, ApJ, 393, 484
Barnes, J. E., & Hut, P. 1986, Nature, 324, 446
Bekenstein, J. 2004, Phys. Rev. D, 70, 083509
Bekenstein, J., & Milgrom, M. 1984, ApJ, 286, 7 (BM84)
Bender, R., Burstein, D., & Faber, S. M. 1992, ApJ, 399, 462
Bernardi, M., et al. 2003a, AJ, 125, 1849
———. 2003b, AJ, 125, 1866
Bertin, G., Ciotti, L., & Del Principe, M. 2002, A&A, 386, 149
Bertin, G., et al. 1994, A&A, 292, 381
Binney, J. 1982, MNRAS, 200, 951
———. 2004, in IAU Symp. 220, Dark Matter in Galaxies, ed. S. D. Ryder et al. (San Francisco: ASP), 3
Binney, J., & Tremaine, S. 1987, Galactic Dynamics (Princeton: Princeton Univ. Press)
Brada, R., & Milgrom, M. 1995, MNRAS, 276, 453
———. 1999, ApJ, 519, 590
———. 2000, ApJ, 541, 556
Caon, N., Capaccioli, M., & D'Onofrio, M. 1993, MNRAS, 265, 1013
Capaccioli, M., Caon, N., & D'Onofrio, M. 1992, MNRAS, 259, 323
Cappellari, M., et al. 2006, MNRAS, 366, 1126
Christodoulou, D. M. 1991, ApJ, 372, 471
Ciotti, L. 1991, A&A, 249, 99
———. 2000, Lecture Notes on Stellar Dynamics (Pisa: Scuola Normale Superiore)
Ciotti, L., & Bertin, G. 1999, A&A, 352, 447
Ciotti, L., & Binney, J. 2004, MNRAS, 351, 285
Ciotti, L., Lanzoni, B., & Renzini, A. 1996, MNRAS, 282, 1
Ciotti, L., Lanzoni, B., & Volonteri, M. 2007, ApJ, 658, 65
Ciotti, L., Londrillo, P., & Nipoti, C. 2006, ApJ, 640, 741 (CLN06)
Ciotti, L., Nipoti, C., & Londrillo, P. 2007, in Collective Phenomena in Macroscopic Systems, ed. G. Bertin et al. (Singapore: World Scientific), in press (astro-ph/0701826)
de Vaucouleurs, G. 1948, Ann. d'Astroph., 11, 247
Dehnen, W. 1993, MNRAS, 265, 250
———. 2002, J. Comput. Phys., 179, 27
Djorgovski, S., & Davis, M. 1987, ApJ, 313, 59
Dressler, A., Lynden-Bell, D., Burstein, D., Davies, R. L., Faber, S. M., Terlevich, R., & Wegner, G. 1987, ApJ, 313, 42
Faber, S. M., & Jackson, R. E. 1976, ApJ, 204, 668
Famaey, B., & Binney, J. 2005, MNRAS, 363, 603
Felten, J. E. 1984, ApJ, 286, 3
Gerhard, O. E., & Spergel, D. N. 1992, ApJ, 397, 38
Graham, A. W., & Guzmán, R. 2003, AJ, 125, 2936
Gunn, J. E., & Gott, J. R. 1972, ApJ, 176, 1
Hockney, R., & Eastwood, J. 1988, Computer Simulation Using Particles (Bristol: Hilger)
Jackson, J. D. 1999, Classical Electrodynamics (New York: Wiley)
Knebe, A., & Gibson, B. K. 2004, MNRAS, 347, 1055
Kormendy, J. 1977, ApJ, 218, 333
Londrillo, P., Messina, A., & Stiavelli, M. 1991, MNRAS, 250, 54
Londrillo, P., Nipoti, C., & Ciotti, L. 2003, Mem. Soc. Astron. Italiana Suppl., 1, 18
Lynden-Bell, D. 1967, MNRAS, 136, 101
Mateo, M. L. 1998, ARA&A, 36, 435
Milgrom, M. 1983, ApJ, 270, 365
———. 1984, ApJ, 287, 571
———. 1994, ApJ, 429, 540
———. 2002, NewA Rev., 46, 741
Nipoti, C., Londrillo, P., & Ciotti, L. 2002, MNRAS, 332, 901
———. 2003, MNRAS, 342, 501
———. 2006, MNRAS, 370, 681 (NLC06)
Nusser, A. 2002, MNRAS, 331, 909
Nusser, A., & Pointecouteau, E. 2006, MNRAS, 366, 969
Plummer, H. C. 1911, MNRAS, 71, 460
Power, C., Navarro, J. F., Jenkins, A., Frenk, C. S., White, S. D. M., Springel, V., Stadel, J., & Quinn, T. 2003, MNRAS, 338, 14
Rees, M. J., & Ostriker, J. P. 1977, MNRAS, 179, 541
Renzini, A., & Ciotti, L. 1993, ApJ, 416, L49
Sanders, R. H. 2000, MNRAS, 313, 767
Sanders, R. H., & McGaugh, S. S. 2002, ARA&A, 40, 263
Sellwood, J. 2004, in IAU Symp. 220, Dark Matter in Galaxies, ed. S. D. Ryder et al. (San Francisco: ASP), 27
Sérsic, J. L. 1968, Atlas de Galaxias Australes (Cordoba: Obs. Astron.)
Shen, S., Mo, H. J., White, S. D. M., Blanton, M. R., Kauffmann, G., Voges, W., Brinkmann, J., & Csabai, I. 2003, MNRAS, 343, 978
Stachniewicz, S., & Kutschera, M. 2005, MNRAS, 362, 89
Tiret, O., & Combes, F. 2007, A&A, in press (astro-ph/0701011)
Tremaine, S., Richstone, D. O., Yong-Ik, B., Dressler, A., Faber, S. M., Grillmair, C., Kormendy, J., & Laurer, T. R. 1994, AJ, 107, 634
Trenti, M., & Bertin, G. 2005, A&A, 429, 161
Trenti, M., Bertin, G., & van Albada, T. S. 2005, A&A, 433, 57
Trujillo, I., Graham, A. W., & Caon, N. 2001, MNRAS, 326, 869
Udry, S. 1993, A&A, 268, 35
van Albada, T. S. 1982, MNRAS, 201, 939
Walker, M. G., Mateo, M., Olszewski, E. W., Pal, J. K., Sen, B., & Woodroofe, M. 2006, ApJ, 642, L41
White, S. D. M. 1978, MNRAS, 184, 185
White, S. D. M., & Rees, M. J. 1978, MNRAS, 183, 341
Zaho, H., & Famaey, B. 2006, ApJ, 638, L9